

# Insight into the electronic structure of the centrosymmetric skyrmion magnet $\text{GdRu}_2\text{Si}_2$

S. V. Eremeev,<sup>1,\*</sup> D. Glazkova,<sup>2</sup> G. Poelchen,<sup>3</sup> A. Kraiker,<sup>4</sup> K. Ali,<sup>5</sup> A. V. Tarasov,<sup>2</sup> S. Schulz,<sup>3</sup> K. Kliemt,<sup>4</sup> E. V. Chulkov,<sup>6,7,8,2</sup> V. S. Stolyarov,<sup>9,10,11</sup> A. Ernst,<sup>12</sup> C. Krellner,<sup>4</sup> D. Yu. Usachov,<sup>2,9,11</sup> and D. V. Vyalikh<sup>8,13,†</sup>

<sup>1</sup>*Institute of Strength Physics and Materials Science,  
Russian Academy of Sciences, 634055 Tomsk, Russia*

<sup>2</sup>*St. Petersburg State University, 7/9 Universitetskaya nab., St. Petersburg, 199034, Russia*

<sup>3</sup>*Institut für Festkörper- und Materialphysik, Technische Universität Dresden, D-01062 Dresden, Germany*

<sup>4</sup>*Kristall- und Materiallabor, Physikalisches Institut, Goethe-Universität Frankfurt,  
Max-von-Laue Strasse 1, D-60438 Frankfurt am Main, Germany*

<sup>5</sup>*Department of Microtechnology and Nanoscience,  
Chalmers University of Technology, Göteborg, 41296 Sweden*

<sup>6</sup>*Departamento de Polímeros y Materiales Avanzados: Física,  
Química y Tecnología, Facultad de Ciencias Químicas,  
Universidad del País Vasco UPV/EHU, 20080 San Sebastián/Donostia, Spain*

<sup>7</sup>*Centro de Física de Materiales (CFM-MPC), Centro Mixto CSIC-UPV/EHU, 20018 San Sebastián/Donostia, Spain*

<sup>8</sup>*Donostia International Physics Center (DIPC), 20018 Donostia-San Sebastián, Spain*

<sup>9</sup>*Moscow Institute of Physics and Technology, Institute Lane 9, Dolgoprudny, Russia*

<sup>10</sup>*Dukhov Research Institute of Automatics (VNIIA), Moscow, 127055 Russia*

<sup>11</sup>*National University of Science and Technology MISIS, Moscow, 119049 Russia*

<sup>12</sup>*Institute for Theoretical Physics, Johannes Kepler University, Linz, Austria*

<sup>13</sup>*IKERBASQUE, Basque Foundation for Science, 48011 Bilbao, Spain*

The discovery of a square magnetic-skyrmion lattice in  $\text{GdRu}_2\text{Si}_2$ , with the smallest so far found skyrmion diameter and without a geometrically frustrated lattice, has attracted significant attention, particularly for potential applications in memory devices and quantum computing. In this work, we present a comprehensive study of surface and bulk electronic structures of  $\text{GdRu}_2\text{Si}_2$  by utilizing momentum-resolved photoemission (ARPES) measurements and first-principles calculations. We show how the electronic structure evolves during the antiferromagnetic transition when a peculiar helical order of  $4f$  magnetic moments within the Gd layers sets in. A nice agreement of the ARPES-derived electronic structure with the calculated one has allowed us to characterize the features of the Fermi surface (FS), unveil the nested region along the  $k_z$  at the corner of the 3D FS, and reveal their orbital compositions. Our findings suggest that the Ruderman-Kittel-Kasuya-Yosida interaction plays a decisive role in stabilizing the spiral-like order of Gd  $4f$  moments responsible for the skyrmion physics in  $\text{GdRu}_2\text{Si}_2$ . Our results provide a deeper understanding of electronic and magnetic properties of this material, which is crucial for predicting and developing novel skyrmion-based devices.

## I. INTRODUCTION

Known since the beginning of the 80s, the centrosymmetric antiferromagnet  $\text{GdRu}_2\text{Si}_2$  ( $T_N$  of  $\sim 46$  K) which crystallizes in the  $\text{ThCr}_2\text{Si}_2$  structure with  $I4/mmm$  space symmetry [1–3] has recently reappeared in the focus of research efforts due to the discovery of a square magnetic-skyrmion lattice without a geometrically frustrated lattice [4]. This skyrmion phase appears in an external magnetic field of 2–2.5 T at temperatures below 20 K. Although magnetic properties of  $\text{GdRu}_2\text{Si}_2$  have been investigated over the years very extensive [1–3, 5–9] the emergence of the skyrmion phase has renewed and intensified the discussions about this material, specifically regarding the reason for and the origin of the skyrmion physics [4, 10–13]. It is worth noting that the discovered square skyrmion lattice has, with a diameter of 1.9 nm,

the smallest skyrmion size ever observed, which makes it attractive for development of next-generation high-density magnetic memory devices with ultralow energy consumption [4, 11].

For further studies of the properties of this material and prediction of possible candidates which could reveal unusual magnetic-skyrmion properties as well, detailed information about surface and bulk electronic structures and, most importantly, on how the electronic structure gets modified upon the antiferromagnetic transition is highly desirable. The latter can be derived from momentum-resolved photoemission (ARPES) measurements combined with *ab initio* calculations. The curious question here is in how far it is possible to detect the stabilization of the helical long-range in-plane magnetic order of Gd  $4f$  moments appearing at zero magnetic field in the ARPES patterns. The next essential question is about the Fermi surface (FS) and its intrinsic properties. Recently, contradicting results were presented for the properties of the three-dimensional (3D) FS. In a recent theoretical study [10], the nested region near the

\* eremeev@ispms.tsc.ru

† denis.vyalikh@dipc.org

$\Gamma$ -point was manifested and it was declared to be responsible for the skyrmion physics in  $\text{GdRu}_2\text{Si}_2$ . However, results of Ref. 14, which also present a detailed overview of the actual discussion about the properties of  $\text{GdRu}_2\text{Si}_2$ , do not confirm the nested region near the  $\Gamma$ -point. This makes a call for a direct experimental visualization of the Fermi surface and further exploration of its properties via ARPES measurements.

Here, we present a detailed study of the electronic structure and discuss FS properties for  $\text{GdRu}_2\text{Si}_2$  obtained from ARPES measurements and *ab initio* density functional theory (DFT) calculations. The latter have been performed for the bulk and for a finite system (slab) that allows us to distinguish surface resonances and surface states for different surface terminations and separate them from the bulk states. Note that most of the surface electron states were observed for the Si-terminated surface of  $\text{GdRu}_2\text{Si}_2$ , where the topmost Gd layer is hidden by the Si-Ru-Si surface trilayer block. In our study, this surface will be of the main focus.

First, our analysis of  $\text{GdRu}_2\text{Si}_2$  will be focused on the characterization of the electronic structure in the paramagnetic phase, which shows a good agreement between experiment and theory. In the AFM ordered phase, our ARPES measurements reveal a pseudogap which is seen as a kind of a "sickle-moon" feature near the Fermi level ( $E_F$ ) in the structure of the bulk projected bands taken along the  $\bar{M} - \bar{X} - \bar{M}$  direction of the surface Brillouin zone (BZ). Our theoretical analysis indicates that this feature is directly linked with the formation of a spiral structure of Gd  $4f$  moments within the basal plane. Further, the agreement between the ARPES-derived electronic structure and the one based on DFT calculations enables a comprehensive characterization of bulk and surface states, including their properties and orbital compositions. Here, we found that in contrast to earlier predictions the FS near the  $\Gamma$ -point does not exhibit nesting properties. Instead, a nesting occurs near the corner of the BZ with a vector along  $[100]([010])$ , which connects  $k_z$ -dispersionless states with noticeable Gd- $d$  contribution. The size of the nesting vector fits well to describe the properties of the spiral magnetic structure. This indicates that the electronic states in this BZ region are most essential for a RKKY-mediated coupling of Gd  $4f$  moments. These results are inline with those recently reported in Ref. 14. Lastly, we discuss results of a theoretical modelling with stretching of the unit cell within the basal plane, analyzing the modifications of the corner-nested region of the BZ. The obtained results allow us to propose the most plausible scenario for the emergence of the helical AFM phase in  $\text{GdRu}_2\text{Si}_2$ .

## II. RESULTS

### A. Calculated electronic structure of the paramagnetic $\text{GdRu}_2\text{Si}_2$ (001) surfaces

We begin with a theoretical analysis of the bulk and surface electronic structure of the paramagnetic  $\text{GdRu}_2\text{Si}_2$  obtained from *ab initio* DFT calculations. Similarly to many others  $\text{RE}_2\text{Si}_2$  materials [15], the predominant cleavage plane of single crystal of  $\text{GdRu}_2\text{Si}_2$  (001) is between Si- and Gd- atomic layers [11], leaving behind an either Si- or Gd-terminated surface. Therefore, to determine surface electron states and separate them from bulk electron bands, an asymmetric slab terminated by Si and Gd on either side was used allowing us to trace bulk-like bands, band gaps as well as surface-related states for both terminations. The in this way theoretically derived electron states for the Gd and Si surfaces of the  $\text{GdRu}_2\text{Si}_2(001)$  are shown in Fig. 1(a, b), respectively. The surface electron states are shown in blue overlaid with the tan-colored  $k_z$ -projected bulk states. The strongly localized Gd  $4f$  orbitals were treated as a frozen core approximation.

Both surfaces reveal a number of surface-related electron states. While some of them overlap strongly with the bulk bands, others reside within large projected band gaps. As we will see further, the theoretically-derived spectral patterns agree nicely with those obtained in the momentum-resolved photoemission experiment. The in-gap surface states seen for the Si surface are almost fully localized within the topmost trilayer Si-Ru-Si block and are mainly composed of Ru  $4d$  orbitals with different symmetries (lower panel of Fig. 1c). We mark a few examples of such states by the colored (red, lightblue and purple) circles in Fig. 1b and present their density profiles  $|\Psi|^2$  in the upper panel of Fig. 1c. The lack of their overlap with the Gd layer makes these surface states rather insensitive to the stabilization of a spin-spiral magnetic order in the AFM phase of  $\text{GdRu}_2\text{Si}_2$ . However, other surface states considerably overlap with the bulk projected states and penetrate into their continuum. Hence, it is reasonable to anticipate that those states, like the one labelled by in green situated between  $\bar{\Gamma}$  and  $\bar{X}$  close to the  $E_F$ , should get modified when the exotic magnetic order on the Gd sublattice sets in. We will discuss the sensitivity of these states to the magnetic order in detail later in comparison with our experimental ARPES results.

### B. ARPES

To comprehensively explore the complex electronic structure of the paramagnetic  $\text{GdRu}_2\text{Si}_2$ , we performed detailed ARPES measurements and compared the obtained results with those derived from our first principle calculations. In the first two rows of Fig. 2, we present the experimentally derived electronic structure taken from

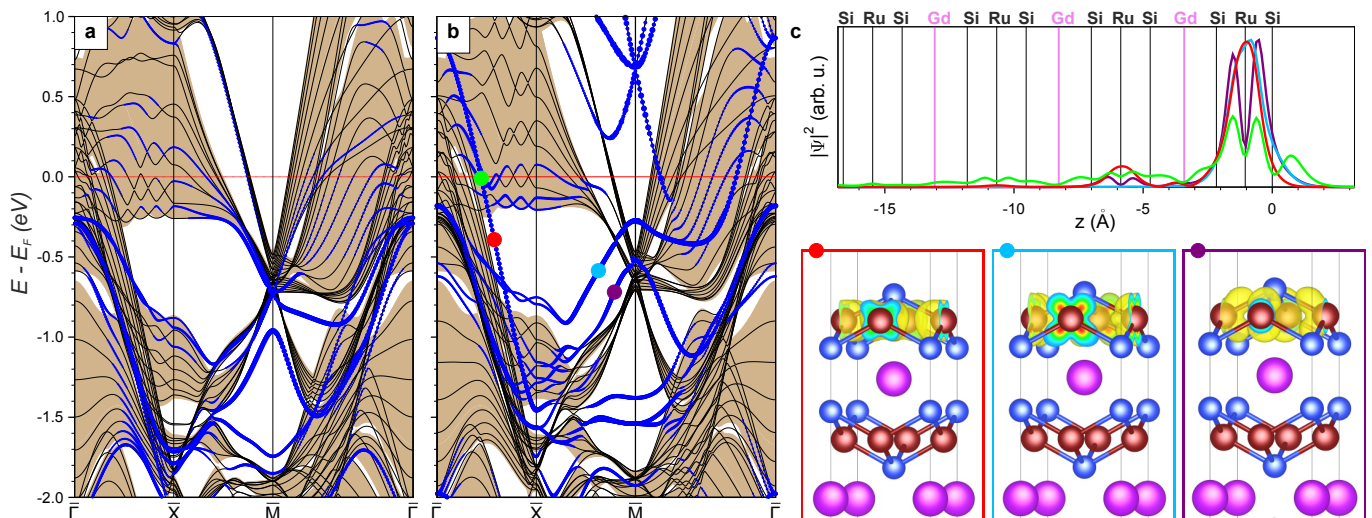


FIG. 1. Electronic structure of the paramagnetic phase of  $\text{GdRu}_2\text{Si}_2(001)$  calculated for Gd- (a) and Si-terminated (b) surfaces. The tan-shaded area corresponds to the surface-projected bulk band structure, whereas the black lines are the result of a slab model. The size of blue dots reflect the weights of the surface states. Large colored circles in (b) mark the states whose spatial distribution is shown in (c) in the same colors. (c) Upper panel: Electron density distribution (integrated over the  $ab$  plane) of the surface electron states marked in (b). Vertical lines reveal the positions of Gd (pink) and Si-Ru-Si (black) atomic layers. Lower panel: spatial distributions for the “red”, “light blue”, and “purple” surface states.

the Si-termination of a freshly cleaved  $\text{GdRu}_2\text{Si}_2$  single crystal at 50 K along the  $\bar{\Gamma} - \bar{M}$ ,  $\bar{\Gamma} - \bar{X}$  and  $\bar{X} - \bar{M}$  directions of the surface BZ. The ARPES pattern were taken at a photon energy of 50 eV with horizontal (LH) and vertical (LV) polarizations shown in the first and second row of Fig. 2, respectively. In the third row, we display the  $k_2$ -projected bulk states along the same high-symmetry directions as in experiment. Similarly to Fig. 1, the tan-colored bulk states are overlaid with the slab-derived surface and surface-resonant states depicted in blue for the paramagnetic, Si-terminated  $\text{GdRu}_2\text{Si}_2$  (001) surface.

The good agreement between experiment and theory allows us to easily identify and differentiate between the surface-related bands and the bulk-projected electronic structure in the ARPES patterns. This gives us a good starting point for the subsequent evaluation of how those states evolve when the peculiar spiral magnetic order of the Gd  $4f$  moments stabilizes in the AFM phase of  $\text{GdRu}_2\text{Si}_2$ . First, we will focus on the bulk states close to  $E_F$ , their properties and orbital composition. Based on Ref. 10, special attention will be paid to the areas near high-symmetry points and in particular on the center of the BZ. Secondly, we will investigate the behavior of the surface-related states which overlap with the bulk states (labelled in green in Fig. 1b). Lastly, we can then discuss and analyse the whole Fermi surface as derived from ARPES measurements and DFT calculations.

### C. Effect of the spin spiral on the electronic structure of $\text{GdRu}_2\text{Si}_2$

After cooling of the  $\text{GdRu}_2\text{Si}_2$  sample below the spiral-AFM phase transition to a temperature of 19 K, we found that the ARPES patterns did not reveal large modifications of the electronic structure. Nevertheless, a number of subtle changes could be observed. One of the most visible changes is the emergence of a narrow bright feature (“pseudogap”) in the bulk-projected spectrum, which can be seen as a kind of “sickle-moon” feature near  $E_F$ . This feature is presented in Fig. 3a in the ARPES data taken along the  $\bar{M} - \bar{X} - \bar{M}$  direction of the surface BZ with the “pseudogap” being indicated by a blue arrow. For comparison, in Fig. 3b we show the projection of the calculated bulk states for the paramagnetic phase onto the same  $\bar{M} - \bar{X} - \bar{M}$  direction of the surface BZ. It clearly demonstrates a homogeneous density of bulk states near the  $\bar{X}$  point in the discussed vicinity of the Fermi level. Having observed the ARPES-derived signature of the spiral-AFM order of the Gd  $4f$  moments, our next step aim was a corresponding appropriate theoretical modeling. Being able to compute and achieve good agreement with experiment would allow us to understand the ground state on the basis of first principles calculations the reasons for such a peculiar magnetic order in the AFM phase of  $\text{GdRu}_2\text{Si}_2$ .

To simulate the spiral-AFM phase, we constructed a bulk  $5 \times 1 \times 1$  supercell, in which the spin spiral corresponding to  $Q = 0.20$  (in units  $2\pi/a$ ) is defined as schematically shown in Fig. 3c. In this supercell the spin magnetic moment on each next Gd plane along the  $x$  direction is rotated by  $\phi = 40^\circ$ . Note that it is

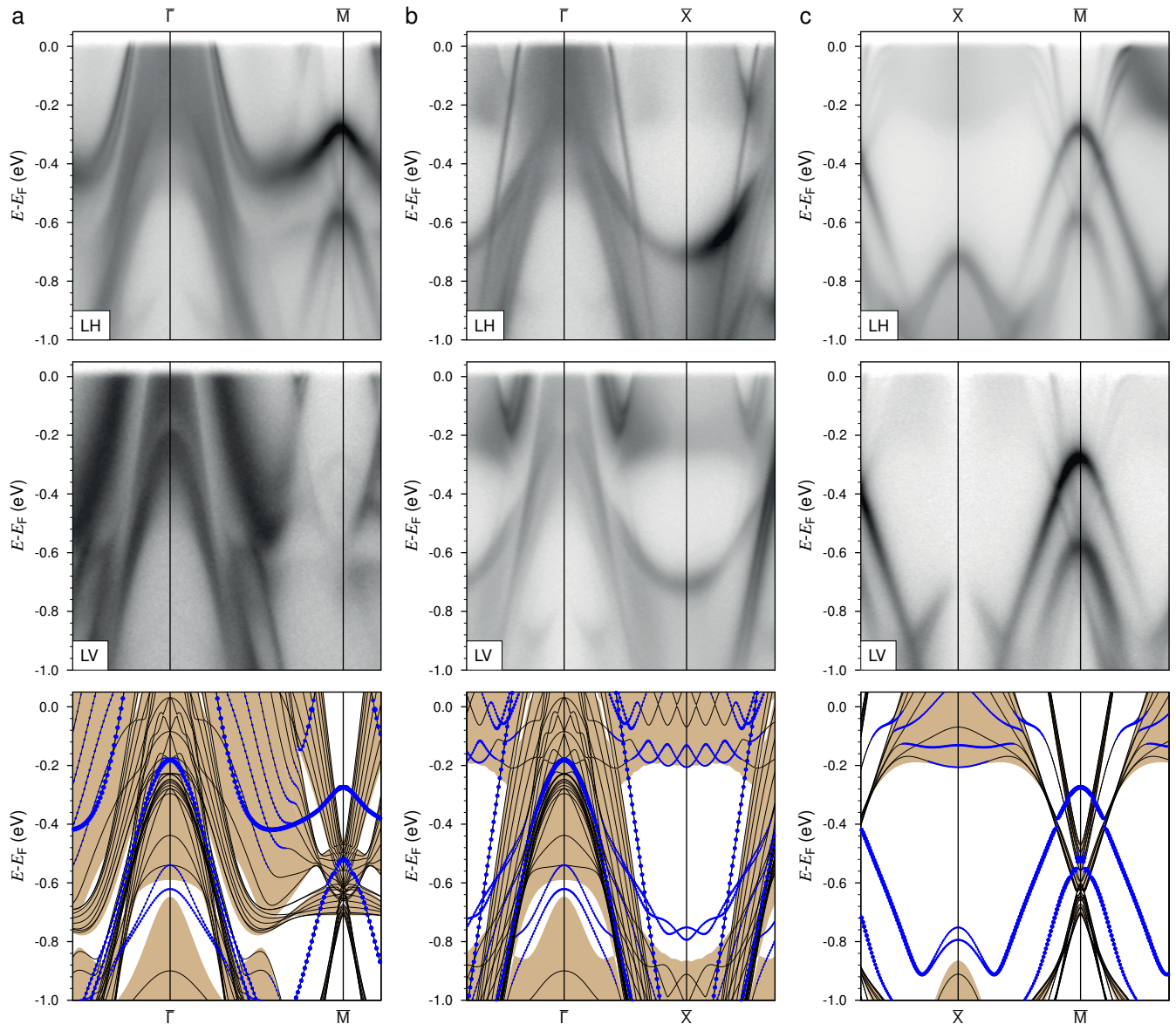


FIG. 2. Comparison between ARPES spectra and DFT-derived band structures for the paramagnetic Si-terminated (001) surface of  $\text{GdRu}_2\text{Si}_2$  along  $\bar{\Gamma} - \bar{M}$  (a),  $\bar{\Gamma} - \bar{X}$  (b), and  $\bar{X} - \bar{M}$  (c) directions measured with linear horizontal (LH) (top row) and linear vertical (LV) (middle row) light polarizations. Bottom row presents the DFT-derived band structure shown in the same energy window for better comparison with ARPES data.

slightly different from  $\phi = 36^\circ$  which corresponds to the experimentally-derived incommensurate spiral propagation vector of  $Q = 0.22$  ( $2\pi/a$ ) [4]. As we will see below the small difference of  $Q = 0.20$  from  $Q = 0.22$  is not essential for the following analysis. The  $k_z$ -projected bulk band structure unfolded onto the  $\bar{M} - \bar{X} - \bar{M}$  direction (perpendicular to the spin spiral propagation, Fig. 3d) of the original  $1 \times 1$  BZ shows that the main changes compared to the paramagnetic case occur close to the  $\bar{X}$  point and near  $E_F$  where density of bulk states becomes inhomogeneous, having an increased density at the very bottom and a reduced one at  $E_F$ . The spectrum calculated along the  $\bar{M} - \bar{Y} - \bar{M}$  direction (along the spin spiral

propagation, Fig. 3e) also demonstrates its main changes at  $\bar{Y}$  (which is equivalent to  $\bar{X}$  in the original  $1 \times 1$  BZ in the paramagnetic case) however, the reduced density can be found here at lower energies while the increased density lies at higher energies closer to  $E_F$ . Taking into account that the magnetic spirals along  $x$  and  $y$  directions must be equiprobable due to symmetry reasons, and that ARPES should acquire a mixture of magnetic domains with different spiral directions, the superposition of the spectra calculated for directions along and perpendicular to the magnetic spiral is presented in Fig. 3f, which shows the presence of a pseudogap in the continuum of the bulk states below  $E_F$  (a narrow area of a reduced density of

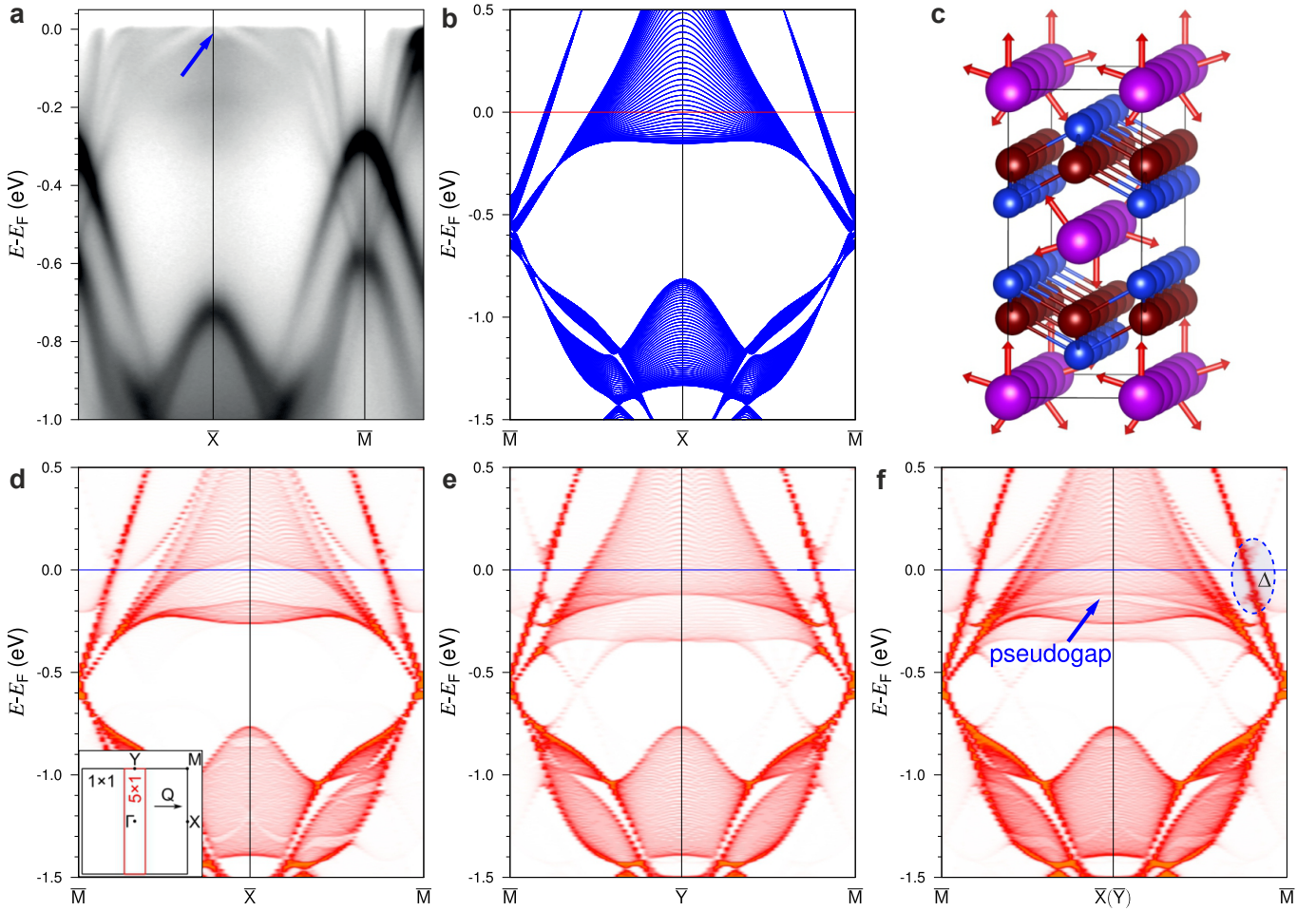


FIG. 3. (a) Low-temperature ARPES data taken at 19 K along the  $\bar{M} - \bar{X} - \bar{M}$  direction of the surface BZ in the AFM phase of  $\text{GdRu}_2\text{Si}_2$ . A blue arrow indicates the “sickle-moon” shaped pseudogap which appears in the bulk continuum states below  $T_N$ . (b) Bulk electron states for the paramagnetic  $\text{GdRu}_2\text{Si}_2$  computed along the  $\bar{M} - \bar{X} - \bar{M}$  direction and projected along  $k_z$ . (c) The  $5 \times 1 \times 1$  supercell of  $\text{GdRu}_2\text{Si}_2$  in the ordered phase where the Gd 4f moments are rotated within the  $yz$ -plane with the propagation vector of  $Q = 0.2$  (in units  $2\pi/a$ ), along the  $x$  direction. (d) The bulk-projected electron structure of the spiral-AFM ordered  $\text{GdRu}_2\text{Si}_2$  calculated within the  $5 \times 1$  supercell with the spin spiral propagated along  $x$  unfolded onto the  $\bar{M} - \bar{X} - \bar{M}$  direction of the original  $1 \times 1$  BZ. The inset shows the  $1 \times 1$  (black) and  $5 \times 1$  (red) BZs projected on (001). (e) The same as in panel (d) but for  $\bar{M} - \bar{Y} - \bar{M}$  direction. (f) Superposition of the bulk projected electron states shown in panels (d) and (e). The meaning of the highlighted  $\Delta$  will be discussed later (see Fig. 6d,e).

the bulk states). This is in excellent agreement with the experiment. Thus, the observation serves as a direct photoemission evidence for the presence of the spiral-AFM phase in the low-temperature limit.

#### D. Electronic structure of the Si-terminated surface of the spiral-AFM $\text{GdRu}_2\text{Si}_2$

Next we explore how the spin-spiral AFM order is reflected in the properties of the surface electrons states, in particular for the Si-terminated surface of  $\text{GdRu}_2\text{Si}_2$ . Fig. 4a and Fig. 4b show the ARPES data taken along the  $\bar{\Gamma} - \bar{X}$  direction in the paramagnetic and spiral-AFM phase, respectively.

The spectra reveal prominent bands located in the en-

ergy range of  $-0.2$  eV up to and crossing  $E_F$ . Our calculations allow us to identify these bands as surface resonances, which penetrate deep into the material overlapping with the bulk band states (Fig. 1b and c, marked in green). Below the spiral-AFM transition these states exhibit notable changes. Particularly, in the paramagnetic phase the photoemission intensity of these states varies smoothly along the spectral structure, while at low temperature a oscillatory modification of the intensity distribution can be observed. To reveal the origin of this intensity redistribution, we expand the  $5 \times 1$  supercell bulk calculation to a supercell slab calculation for the spiral-AFM phase. Fig. 4c shows the spectrum of the Si-terminated (001) surface of  $\text{GdRu}_2\text{Si}_2$  unfolded onto the  $\bar{\Gamma} - \bar{X}$  (along the propagation of the spin spiral) and the  $\bar{\Gamma} - \bar{Y}$  (perpendicular to the spin spiral) directions of the

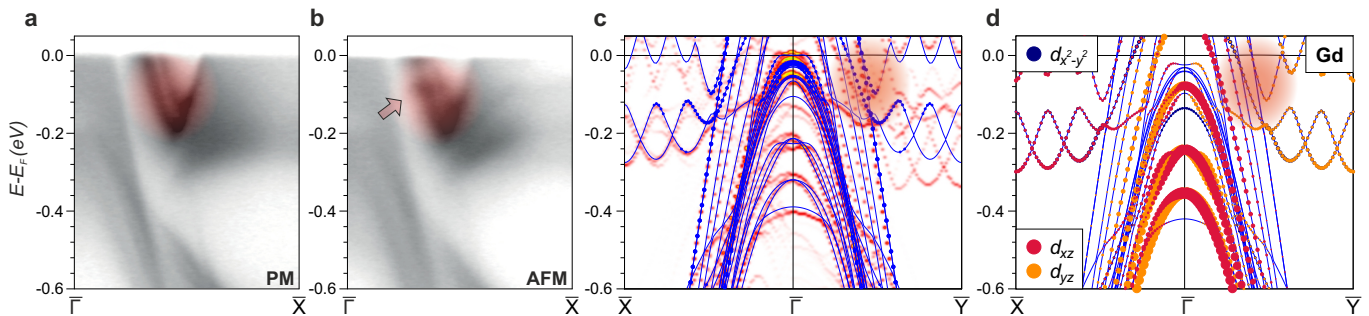


FIG. 4. ARPES data taken along the  $\bar{\Gamma} - \bar{X}$  direction at 50 K (a) and at 19 K (b), that is, above and below the bulk  $T_N$ , respectively. The measurements were performed using a photon energy of 50 eV with linear vertical (*s*) polarization. The orange highlighted spot marks an area of the surface resonant state. (c) Unfolded calculated spectrum (shown in red) of the Si-terminated GdRu<sub>2</sub>Si<sub>2</sub> (001) surface for the spiral-AFM phase along  $\bar{\Gamma} - \bar{X}$  (along the propagation of the spin spiral) and  $\bar{\Gamma} - \bar{Y}$  (perpendicular to the spin spiral) directions. The spectrum of the GdRu<sub>2</sub>Si<sub>2</sub> slab of the same thickness for the paramagnetic phase is imposed (blue curves) and weights of the surface states demonstrated by blue dots. (d) Weights of the Gd-5*d* orbitals for the paramagnetic phase.

$1 \times 1$  BZ. Compared to the band structure of the paramagnetic phase (blue lines in Fig. 4c), both electronic structures almost coincide for the direction of the spiral propagation ( $\bar{\Gamma} - \bar{X}$ ), whereas in the perpendicular direction ( $\bar{\Gamma} - \bar{Y}$ ) the band distribution considerably changes.

Near  $E_F$ , the Gd-5*d* contribution to these states is almost equally determined by  $d_{x^2-y^2}$  and  $d_{xz}(d_{yz})$  orbitals (see the Fig. 4d). With the spin spiral propagating along the *x* direction, the spin rotates in the *yz*-plane and clearly affects the  $d_{yz}$  orbitals but seems to have no influence on the  $d_{xz}$  orbital. Hence, when the surface resonant state penetrates into these bulk states, where the weight of Gd-5*d* orbitals is considerable, it should experience the effect of spiral-AFM order in the bulk. Again, due to the mixture of *x*- and *y*-spiral magnetic domains, in ARPES this modification manifests itself in both  $\bar{X} - \bar{\Gamma}$  and  $\bar{\Gamma} - \bar{X}$  directions leading to a subtle but clearly notable effect.

### E. Fermi surface and possible origin of the spin spiral

In Ref. 10, the properties of the three-dimensional FS were intensively discussed. There, it was argued that nesting properties found in the center of the BZ are the key points for the formation of the spin-spiral magnetic order in the AFM phase of GdRu<sub>2</sub>Si<sub>2</sub> and define the skyrmion physics in this material. To explore this point in detail, we present the calculated FS for the paramagnetic phase of GdRu<sub>2</sub>Si<sub>2</sub> (Fig. 5a and b) with the experimentally-derived FS from ARPES measurements (part of Fig. 5c). To simplify the analysis, we combine the ARPES data with the calculated band structure projected along the  $k_z$  direction onto the (001) surface as shown on the left side of Fig. 5c. Based on this comparison, we see a close to perfect agreement between experiment and theory, indicating that our calculations reliably describe all bands in the vicinity of  $E_F$ . The four bands which form the FS are labeled as 1–4.

In Ref. 10 it was proposed that band 3, which is highlighted in red in Fig. 5a,b, is mostly barrel-shaped and therefore provides good nesting conditions where the diameter of the barrel fits well to the wave number  $Q = 0.22 (2\pi/a)$  of the spin spiral. We indicate the respective region by a blue arrow around the  $\bar{\Gamma}$  point in Fig. 5c. However, based on our DFT results, we offer a different interpretation. First, we find that band 3 differs considerably more from a barrel-like shape than previously proposed and instead looks more ellipsoidal with a significant  $k_z$  dispersion centered around the Z-point of the BZ. In this regard, our calculation suggest that there are no strong nesting properties for this band.

On the other hand, our calculations indicate that band 4, which is situated around the  $\bar{M}$  point, reveals nesting properties. This band shows almost no  $k_z$ -dispersion in the  $\bar{M} - \bar{X}$  lateral direction. To better visualize this fact, we present in the outset of Fig. 5b the discussed band 4 from the top perspective. In this top view projection, it is clearly visible that the  $\bar{M} - \bar{X}$  cuts have no  $k_z$  dispersion since they meet in single points. This nesting vector is highlighted by a red arrow at the corner of BZ in the FS shown in Fig. 5c. Further, it is important to note that these points have a high density of states and possess a strong contribution from Gd 5*d* states, which are essential for the exchange interaction and will be discussed next.

To understand the relation between the spiral period and the features of the band structure, we analyze the orbital composition of the bands 1–4 at  $E_F$ . As illustrated in Fig. 6a, bands 1 and especially 4 have strong contributions from Gd 5*d* states, while bands 2 and 3 are mainly composed of Ru states with only a small contribution from Gd states (see detailed analysis of the orbital composition in the Appendix, Section 1). This allows us to conclude that band 4 not only fulfills the nesting condition, but also has the most significant admixture from Gd 5*d*-states, and thus is the most likely origin for the peculiar magnetic structure of GdRu<sub>2</sub>Si<sub>2</sub>.

Next, we will test the relation between the nesting vec-

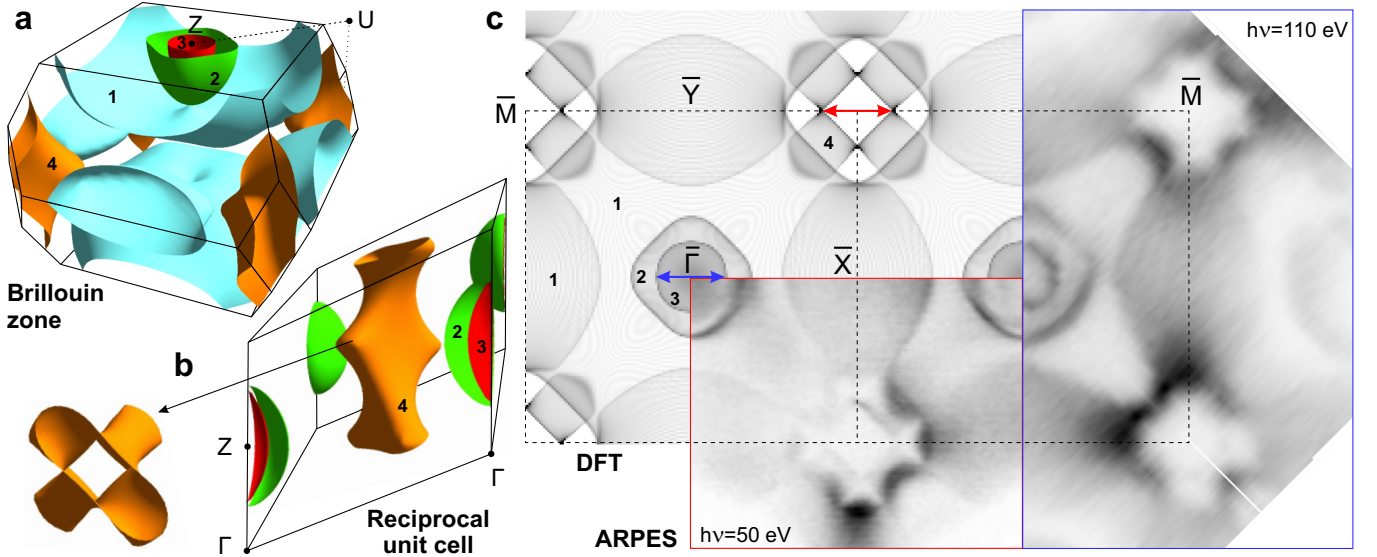


FIG. 5. Fermi surface (FS) for  $\text{GdRu}_2\text{Si}_2$  in the paramagnetic phase presented for the first BZ (a) and for the reciprocal lattice unit (b). In panel (b), band 1 is not shown for simplicity; the left outset shows the top perspective view of band 4. (c) Projection of the calculated FS on the (001) surface. The red and blue framed parts show the ARPES-derived FS maps taken with photon energies of  $h\nu = 50 \text{ eV}$  and  $h\nu = 110 \text{ eV}$ , respectively. The red arrow indicates the proposed nested region in the 3D FS while the blue arrow shows the region near the center of the BZ, which was discussed in Ref. 10.

tor and the spiral period. For that, we performed a series of ab-initio calculations where the crystal lattice was stretched or compressed within the  $ab$  plane. Such deformations may lead to significant changes of the band structure as well as the spiral period, providing a possibility to explore the relationship between them. Fig. 6b demonstrates how the total energy evolves as a function of the spiral wave number  $Q$  for different values of stretching. Note that the shown curves are arbitrarily shifted in the energy scale for better comparison. For the case of the equilibrium lattice (black curve), the energy minimum is located at  $Q = 0.20$ , which is very close to the experimental value of  $Q = 0.22$ . Upon expansion of the lattice the minimum shifts to lower  $Q$  values until the system becomes ferromagnetic which happens at 11% of stretching. Upon compression of the lattice the global energy minimum turns to a local minimum, which shifts towards higher  $Q$  values and almost disappears already at 2.5% of compression.

We can now determine how the band structure evolves under lattice deformation. For this, we will look in detail at the two most interesting bands, namely band 4, which we propose to be responsible for the spiral-AFM order since it exhibits strong nesting properties, and band 3, which was proposed in Ref. 10. What we observe as a result of stretching is that band 4 shifts up in energy, while band 3 gets shifted down to lower energies. In both cases the related nesting vector becomes shorter, which is illustrated in Fig. 6c where the lengths of the proposed nesting vectors are shown as function of stretching. The nesting vectors were measured along the  $Z$ - $U$  direction of the BZ shown in Fig. 5a. Our results indicate a qualita-

tive correlation between the length of the nesting vectors and the wave number of the spiral. Upon stretching, the nesting vector gets shorter for both bands 3 and 4, while in the same way the spiral wave number becomes smaller. However, the experimental value of the wave number  $Q = 0.22$  ( $2\pi/a$ ) for the equilibrium lattice fits better to the nesting vector of band 4 than band 3 (experimental value shown as green star in Fig. 6c). Additionally, the stretching value at which band 4 shifts above  $E_F$  coincides with the stretching value of 11% where the calculated  $Q$  becomes zero. Thus, in agreement with our previous statements about band 4, this band seems to be the probable candidate for the formation of the spin spiral via  $d-f$  hybridization.

To understand further the role of band 4 in the stabilization of the spiral state, we present the theoretical band structure of the spiral-AFM state in Fig. 6d. These calculations were performed using a so-called generalized Bloch condition. In this formalism, for the case of a rotating spin, the wave function has the form of the following spinor

$$\Psi(\vec{r}) = \frac{1}{\sqrt{2}} \sum_{\vec{R}} \begin{pmatrix} e^{i(\vec{k}-\vec{Q}/2)\cdot\vec{R}} \phi^\uparrow(\vec{r}-\vec{R}) \\ e^{i(\vec{k}+\vec{Q}/2)\cdot\vec{R}} \phi^\downarrow(\vec{r}-\vec{R}) \end{pmatrix}, \quad (1)$$

summing over all unit cells. To ensure a spin rotation, the quasi-momentum  $\vec{k}$  gains an additional quantity of  $\pm\vec{Q}/2$  that results in the respective translation of bands in the reciprocal space. This is schematically illustrated in Fig. 6e. In the paramagnetic phase, the states of band 4 at  $E_F$  at the two sides of the M point are separated by the nesting vector  $\vec{Q}$  which coincides with the spin spiral

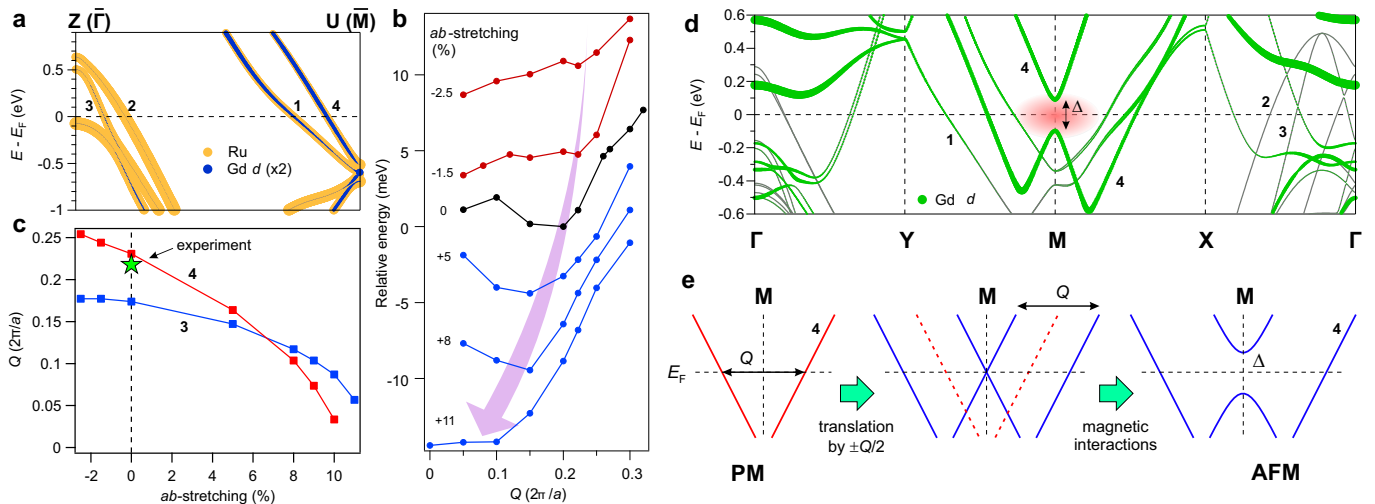


FIG. 6. (a) Electron band structure near the  $E_F$  calculated along the Z-U direction of the BZ (see Fig. 5a); the size of the colored symbols represents the weight of all states of Ru and  $5d$  states of Gd, where the weight for the latter is multiplied by a factor of two. (b) The evolution of the total energy of the tetragonal cell as a function of the spin-spiral wave number  $Q$ . The cartoon arrow indicates how the minimum of total energy evolves upon the lattice stretching. (c) Calculated evolution of the lengths of the red and blue  $\vec{k}$  vectors shown in Fig. 5c for the bands 3 and 4 at  $E_F$ . (d) Band structure for the spiral-AFM state with  $Q = 0.22$  ( $2\pi/a$ ), calculated using the tetragonal unit cell (the spiral vector  $\vec{Q}$  is parallel to the  $\Gamma - X$  and  $Y - X$  directions). (e) Schematic illustration of the formation of the band 4 in the direction along the spiral.

wave vector. Upon translation by  $\pm\vec{Q}/2$  the two sides of the band cross at the M point. The exchange interaction results in opening of a magnetic gap  $\Delta$  at the M point. The related decrease in the energy of the occupied states results in stabilization of the spiral. At the same time, bands 2 and 3 remain almost unchanged due to their small contribution of the Gd  $5d$  orbitals.

It is worth noting that an experimental observation of the predicted magnetic gap with ARPES is very challenging. First, the band structure in Fig. 6d cannot be directly compared with ARPES data because of the redefinition of the quasimomentum  $\vec{k}$ . The experimental measurements have to be compared with the unfolded bands from the supercell calculations shown in Fig 3f. One can see that the discussed gap  $\Delta$  in the band 4 is present in the supercell calculation, although it appears shifted by  $\vec{Q}/2$  from the  $\bar{M}$  point. Moreover, it does not look like a real gap since it is formed only between the low-intensity replica bands which cannot be reliably detected in our ARPES data. Instead, we were able to detect the aforementioned pseudogap formed in band 1 that is of magnetic origin and thus indicates the formation of the spiral-AFM state.

## F. Magnetic interaction

To understand in more details the nature of magnetic interaction in the system, we calculated exchange coupling constants from first-principles applying the magnetic force theorem as it is implemented within the multiple scattering theory [16, 17]. The exchange coupling

constants,  $J_{ij}$  represent the direct and indirect overlap between wave functions participating in the magnetic interaction between atoms  $i$  and  $j$ . A full Fourier transform,  $J(\vec{Q})$  is proportional the total energy, which minimum, i.e. the ground state, corresponds to the maximum of  $J(\vec{Q})$ . To determine the ground state,  $J(\vec{Q})$  was computed along high symmetry directions of the BZ using various density functional approximations. The HSE06 hybrid functional is the best approach for describing the the magnetic bulk band structure of  $\text{GdRu}_2\text{Si}_2$  (see discussion in the Appendix, Section 1). Unfortunately, this method is not yet implemented within the multiple scattering theory. Therefore, we used a GGA+ $U$  functional to obtain exchange coupling constants. It should be noted that previously reported first-principles studies of this system were carried out using a bare GGA functional [10, 12]. Unfortunately, the GGA+ $U$  approximation can not fully reproduce the band structure obtained with the HSE06 hybrid functional. Nevertheless, the Gd  $4f$  states are pushed down in energy within this approaches and the band structure in the Fermi level vicinity with exception several features looks similar to that obtained within the HSE06 (Appendix, Section 1, Fig. 7).

$J(\vec{Q})$  calculated along the high symmetry directions show three peaks: one is between  $\Gamma$  and X, the second is between X and M, and the third is between  $\Gamma$  and Z (see the Appendix, Section 2, Fig. 8a). The global maximum, which corresponds the total energy minimum, determines a spiral magnetic structure within the Gd layer. The  $Q$  vector of this maximum is in a good agreement with our calculations within generalized Bloch conditions and experiment. However the presence of two other peaks



with similar magnitudes indicates a competition between three various magnetic orders: two intra- and one inter-layer spirals. We point here that the results might be not fully correct, since the used approximation does not provide a full agreement with the HSE06 hybrid functional calculations. Another approach we have tried, a self-interaction correction (SIC) method, delivers a similar picture (see the Appendix, Fig. 8b), although  $J(\vec{Q})$  are about two times smaller than that obtained within the GGA+ $U$  approach. The later fact is because the SIC method overestimates usually localization of SI-corrected orbitals. However, both approaches predict a similar magnetic structure.

The next question arises of the origin of spirals in GdRu<sub>2</sub>Si<sub>2</sub>. A structurally similar system, GdRh<sub>2</sub>Si<sub>2</sub>, exhibits a robust layerwise antiferromagnetic ordering with the relatively high Néel temperature of 107 K [18]. We think there are two main reasons for so strong difference between these two AFM materials. First, Rh has one  $4d$  electron more than Ru. Therefore, Rh-Si hybridization is essentially distinct from that between Ru and Si atoms. The additional Rh  $4d$  electron weakens the Gd-Si coupling and Gd has more  $5d$  electrons for the intra-layer magnetic coupling between the Gd  $4f$  local moments, which results in a strong ferromagnetic order within the Gd layers. Indeed, the magnetic interaction between the nearest Gd moments in GdRh<sub>2</sub>Si<sub>2</sub> is much stronger than that in GdRu<sub>2</sub>Si<sub>2</sub>: 5.1 meV vs. 0.7 meV, while the inter-layer magnetic coupling in both system is of a similar magnitude. The second reason for the stronger intra-layer coupling in GdRh<sub>2</sub>Si<sub>2</sub> is the slight difference in the lattice parameters in these materials. Lanthanides are well known for a sensitive dependence of their magnetic properties on the structure. Thus, a strong reduction of the intra-layer magnetic interaction in GdRu<sub>2</sub>Si<sub>2</sub> leads to magnetic frustration and spiral formation in this material. Our analysis indicates that the magnetic interaction between Gd  $4f$  local moments is mainly mediated by conduction electrons. Although our ARPES experiments and DFT calculations do not confirm the nesting found in Ref. [10], the magnitude of the respective vector which was discussed in Ref. [10] is similar to the nesting vector at the corner of BZ which was found in our study. Combining our finding and the discussion made in Ref. [10] we conclude that the RKKY interaction is the dominant mechanism for helical magnetism in this system.

### III. CONCLUSIONS

In summary, applying momentum-resolved photoemission measurements and *ab-initio* DFT calculations, we explored the bulk and surface electronic structure of the helical antiferromagnetic material GdRu<sub>2</sub>Si<sub>2</sub>. The ARPES-derived data, taken for GdRu<sub>2</sub>Si<sub>2</sub> in paramagnetic phase, reveal a sharp patterns containing the surface and bulk-projected electron states which allow to explore how these states are modified upon the PM-AFM

phase transition. Note that in difference to many recently studied RET<sub>2</sub>Si<sub>2</sub> non-helical antiferromagnets [15], the surface states of Si-terminated GdRu<sub>2</sub>Si<sub>2</sub> do not reveal notable exchange splittings. The latter is mainly because these states are localized on the Ru layer in Si-Ru-Si surface block. Comparison of the ARPES data taken from the AFM phase of GdRu<sub>2</sub>Si<sub>2</sub> with the results of *ab-initio* DFT calculations allowed us to find bulk-related spectral features which are intrinsic for the spiral's order of  $4f$  moments. Namely, we detected a pseudogap within the bulk continuum states close to  $E_F$  which is seen as a “sickle-moon” shaped spectral feature. A rather good agreement of experimental and theoretical results allowed us to characterize in detail the properties and orbital composition of the Fermi surface of GdRu<sub>2</sub>Si<sub>2</sub>. Note that our results do not confirm the prediction of the existence of the nested three-dimensional barrel-shaped FS near the  $\Gamma$ -point which was reported recently [10]. Instead, we found a nested FS sheet at the corner of the BZ, supporting the recent results reported in Ref. 14. Our theoretical analysis suggests that this feature possesses a strong admixture of  $5d$ -states of Gd. We show that stretching or compressing the crystal lattice within the *ab* plane essentially influences the Gd  $5d$  states nesting vector and consequently changes the period of the magnetic spiral in the Gd  $4f$  spin channel. The obtained results allow us to conclude that the RKKY interaction is the most plausible mechanism which defines the spiral magnetic order in GdRu<sub>2</sub>Si<sub>2</sub> and is responsible for the emergence of skyrmions in this material.

### METHODS

Single crystals of GdRu<sub>2</sub>Si<sub>2</sub> were grown from indium flux using high purity starting materials Gd (99.9%, EvoChem), Ru (99.95%, EvoChem), Si (99.9999%, Wacker) and In (99.9995%, Schuckard) and a modified Bridgman method as described in [19]. Gd, Ru, Si, and In were used in the ratio of Gd : Ru : Si : In = 1 : 2 : 2 : 24. The crystal growth was performed in a vertical furnace (GERO HTRV 70-250/18) ( $T_{max} = 1600^\circ\text{C}$ ), a slow cooling period with a rate of 1–4 K/h down to 850°C followed by fast cooling to room temperature with 300 K/h. The crystals were separated from the flux by etching in hydrochloric acid. We obtained platelet-shaped crystals with typical dimensions of 3 mm × 3 mm and a thickness of 50 – 100  $\mu\text{m}$ .

ARPES experiments were first performed at the ULTRA endstation of the SIS-X09LA beamline, Swiss Light Source, in November 2021. Additional detailed high-quality measurements were obtained in a second measurement at the BLOCH beamline, MAX-IV laboratory, in July 2022. Both ARPES endstations were equipped with a Scienta R4000 analyzer. The single-crystal samples of GdRu<sub>2</sub>Si<sub>2</sub> were cleaved *in situ* under ultra-high vacuum conditions better than  $10^{-10}$  mbar.

Electronic structure calculations were carried out

within the density functional theory using the projector augmented-wave (PAW) method [20–22] as implemented in the VASP code [23, 24]. The exchange-correlation energy was treated using the generalized gradient approximation [25] for most calculations. The trivalent Gd potential (when strongly localized valence  $4f$  electrons are treated as core states) was used for non-magnetic calculations. The standard tetravalent Gd potential in which the  $4f$  electrons are treated as valence states was used for spin-polarized calculations of magnetic phases. To correctly describe the highly correlated Gd- $4f$  electrons, we include the correlation effects within both the HSE06 screened hybrid functional [26] and the GGA+ $U$  method [27]. The values of  $U$  and  $J$  parameters were taken to be of 6.7 eV and 0.7 eV, respectively, which give a good agreement with HSE06 band structure. Additionally we use Slater-type DFT-1/2 self-energy correction method [28, 29] with a partially (quaternary) ionized silicon potential for better describing hybridization between deep Gd- $f$  and Si- $p_{xy}$  orbitals. To simulate the spiral magnetic state we consider spin spirals with two different methods. The first is to construct explicitly the spiral in supercell using noncollinear magnetic moments in the  $yz$ -plane, perpendicular to the spin spiral propagation vector (along  $x$  direction) and the second approach is to use a spin spiral method to simulate spirals in the unit cell with generalized Bloch conditions [30]. In the first case we use BandUP code [31, 32] to unfold the supercell band structure onto  $1 \times 1$  BZ. Additional band structure calculations for the paramagnetic phase (Fig. 5c) were performed with the Gd  $4f$  states in the core using FPLO-18.00-52 code (improved version of the original FPLO code by K. Koepernik and H. Eschrig [33]). The results are in perfect agreement with those obtained with the VASP code. All presented ball-and-stick atomic structures were visualized with VESTA [34]. The Fermi surface was determined on a dense  $27 \times 27 \times 23$   $k$ -point mesh and visualized by using FermiSurfer [35].

## ACKNOWLEDGEMENTS

We acknowledge the German Research Foundation (DFG) for the support through the grants No. KR3831/5-1, No. LA655/20-1, SFB1143 (Project No. 247310070), and TRR288 (No. 422213477, Project No. A03). The density functional theory calculations were supported by the Government research assignment for ISPMS SB RAS (Project FWRW-2022-0001). E.V.C. acknowledges support from Saint Petersburg State University (Project ID No. 94031444). V.S.S. and D.Yu.U. work was partially supported by the Ministry of Science and Higher Education of the Russian Federation (No. FSMG-2023-0014) and RSF 23-72-30004. The calculations were partially performed using the equipment of the Shared Resource Center “Far Eastern Computing Resource” of IACP FEB RAS (<https://cc.dvo.ru>) and Joint Supercomputer Center of the Russian Academy of

Sciences (<https://rscgroup.ru/en/project/jscc>). We also thank the Paul Scherrer Institut, Villigen, Switzerland for the allocation of ARPES experiments at the ULTRA endstation of the SIS-X09LA beamline of the Swiss Light Source. We acknowledge MAX IV Laboratory for experimental time on Beamline BLOCH under Proposal 20211066. Research conducted at MAX IV, a Swedish national user facility, is supported by the Swedish Research Council under contract 2018-07152, the Swedish Governmental Agency for Innovation Systems under contract 2018-04969, and Formas under contract 2019-0249.

## APPENDIX

### 1. Calculated bulk band structure

To reveal the band structure of GdRu<sub>2</sub>Si<sub>2</sub> with helical AFM magnetic structure, we started from paramagnetic calculation where trivalent Gd potential is used in which strongly localized valence  $4f$  electrons are treated as core states (Fig. 7a). The spectra of paramagnetic phase calculated along high symmetry directions of the bulk Brillouin zone (Fig. 7a, top) using the Heyd-Scuseria-Ernzerhof (HSE06) screened hybrid functional [26] and that obtained within bare GGA-PBE calculation are demonstrated in Figs. 7 a and b, respectively. As can be seen from comparison of these spectra the latter one does not reproduce well the more accurate HSE06 result, especially at the Fermi level. Applying DFT-1/2 corrections over GGA-PBE allows receiving more accurate description of the nonmagnetic spectrum in this energy range (Fig. 7d). Scalar-relativistic spectrum of AFM GdRu<sub>2</sub>Si<sub>2</sub> was calculated with tetravalent Gd potential in which the  $4f$  electrons are treated as valence states within the HSE06 approach (Fig. 7e). Fig. 7e also presents projections of weights of the Gd, Ru, and Si orbitals (left, middle, and right subpanels, respectively). As can be seen the Gd  $4f$  localized band, located at  $\sim -7.5$  eV, hybridizes with Si  $p_{xy}$  orbitals. Si  $s$  and  $p_z$  states contribute to the bottom of the main valence band, which is mainly formed by Ru  $d$  orbitals. However, the Gd  $d$  states also present near the Fermi level ( $E_F$ ) where they have most pronounced weights in the vicinity of the M point. Thus we can conclude the Gd  $d$  are the orbitals which mediate magnetization of the bulk bands near the Fermi level via Gd  $f - d$  hybridization. To mimic the HSE06 band structure the simplified GGA+ $U$  approach was applied (see details in the Method section). The GGA+ $U$  spectrum as obtained within PBE calculation reasonably well reproduces the position of the Gd  $f - d$  band (Fig. 7f). However, like in the nonmagnetic case, the spectrum at  $E_F$  differs from that calculated within HSE06 approach as well as position of the deep Si  $p_{xy}$  states. The partial ionization of Si potential within DFT-1/2 method resolves both these problems (Fig. 7g).

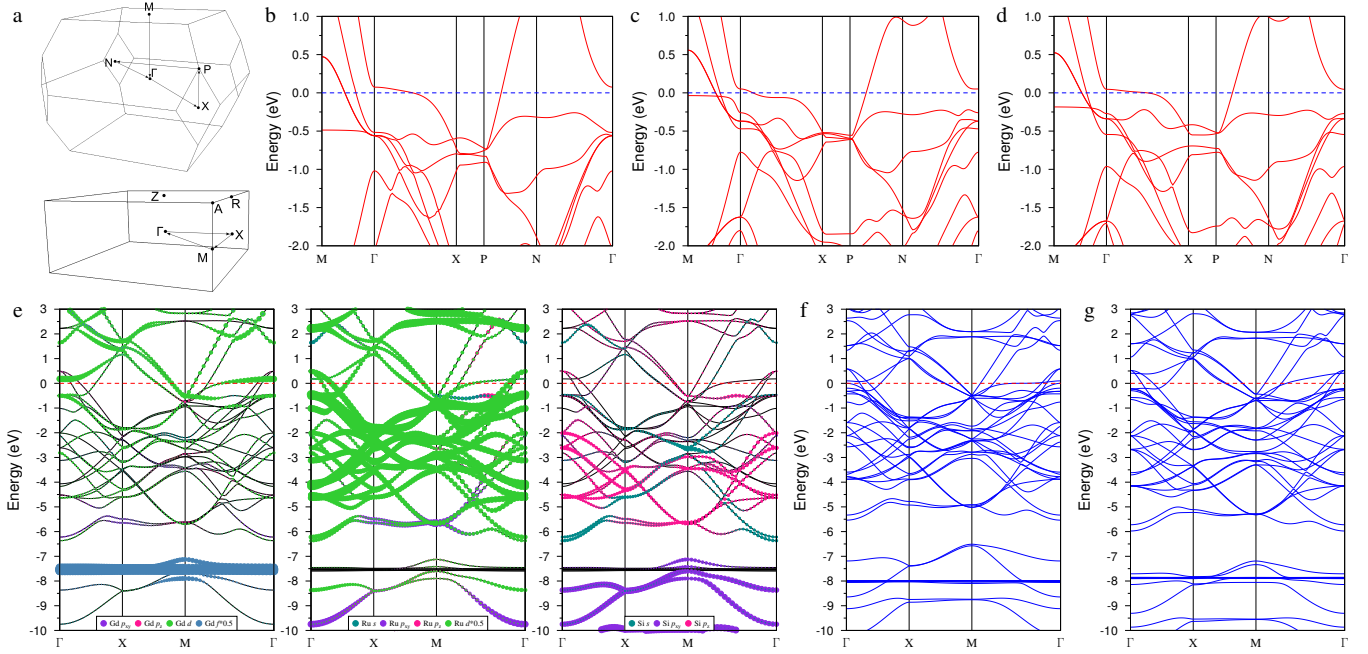


FIG. 7. (a) Bulk Brillouin zones for paramagnetic primitive (top) and for AFM tetragonal (bottom) cells. Arrows show the paths along which electronic spectra are calculated. (b) Bulk energy spectrum of paramagnetic  $\text{GdRu}_2\text{Si}_2$  where Gd states are treated as core electrons as obtained with HSE06 hybrid functional. (c) The spectrum of nonmagnetic  $\text{GdRu}_2\text{Si}_2$  calculated within bare GGA-PBE approach. (d) The same but within DFT-1/2 approach. (e) Scalar-relativistic spectrum of AFM  $\text{GdRu}_2\text{Si}_2$  calculated within HSE06 approach with weights of the Gd (left), Ru (middle), and Si (right) orbitals. (f) Scalar-relativistic spectrum of AFM phase calculated within GGA-PBE with  $U = 6.7$  eV and  $J = 0.7$  eV. (g) The spectrum calculated within GGA-PBE with  $U = 6.7$  eV and  $J = 0.7$  eV and quaternary ionized Si  $p$  states within DFT-1/2 approach.

## 2. Magnetic interaction

Exchange constants were calculated using the magnetic force theorem as it is implemented within the multiple scattering theory [16]. To describe localized Gd  $4f$  electrons we used two different DFT functionals, a GGA+ $U$  approach [36] and a self-interaction correction (SIC) method [17, 37, 38]. The results of our calculations

are presented in Fig. 8. Both approaches provide a similar behaviour of  $J(\vec{Q})$  and the  $J(\vec{Q})$  maximum occurs at the same wave vector  $Q \approx 0.2 (2\pi/a)$  along  $\Gamma - X$  direction. However, the magnitude of  $J$ 's calculated within the SIC method is significantly smaller than that obtained using the GGA+ $U$  approximation. The reason is that the SIC method overestimates localization of corrected orbitals. Therefore, in our manuscript we rely on the results obtained within the GGA+ $U$  approach.

- 
- [1] M. Ślaski and A. Szytuła, Crystal structure and magnetic properties of  $\text{REMe}_2\text{Si}_2$  compounds (RE = Gd, Dy, Ho, Er; Me = Ru, Rh, Pd, Ir), *Journal of the Less-Common Metals* **87**, L1 – L3 (1982).
  - [2] K. Hiebl, C. Horvath, P. Rogl, and M. J. Sienko, Magnetic properties and structural chemistry of ternary silicides (RE,Th,U) $\text{Ru}_2\text{Si}_2$  (RE = Rare Earth), *Journal of Magnetism and Magnetic Materials* **37**, 287 (1983).
  - [3] M. Ślaski, A. Szytuła, J. Leciejewicz, and A. Zygmunt, Magnetic properties of  $\text{RERu}_2\text{Si}_2$  (RE=Pr, Nd, Gd, Tb, Dy, Er) intermetallics, *Journal of Magnetism and Magnetic Materials* **46**, 114 (1984).
  - [4] N. D. Khanh, T. Nakajima, X. Yu, S. Gao, K. Shibata, M. Hirschberger, Y. Yamasaki, H. Sagayama, H. Nakao, L. Peng, K. Nakajima, T. Takagi, R. Arima, Y. Tokura, and S. Seki, Nanometric square skyrmion lattice in a centrosymmetric tetragonal magnet, *Nature Nanotechnology* **15**, 444–449 (2020).
  - [5] A. Garnier, D. Gignoux, N. Iwata, D. Schmitt, T. Shigeoka, and F. Zhang, Anisotropic metamagnetism in  $\text{GdRu}_2\text{Si}_2$ , *Journal of Magnetism and Magnetic Materials* **140-144**, 899 (1995).
  - [6] M. Rotter, M. Doerr, M. Zschintzsch, A. Lindbaum, H. Sassik, and G. Behr, The magnetoelastic paradox in  $\text{GdAg}_2$  and  $\text{GdRu}_2\text{Si}_2$ , *Journal of Magnetism and Magnetic Materials* **310**, 1383 (2007).
  - [7] T. Samanta, I. Das, and S. Banerjee, Comparative studies of magnetocaloric effect and magnetotransport behavior in  $\text{GdRu}_2\text{Si}_2$  compound, *Journal of Applied Physics* **104**, 123901 (2008).
  - [8] A. Garnier, D. Gignoux, D. Schmitt, and T. Shigeoka, Giant magnetic anisotropy in tetragonal  $\text{GdRu}_2\text{Ge}_2$  and

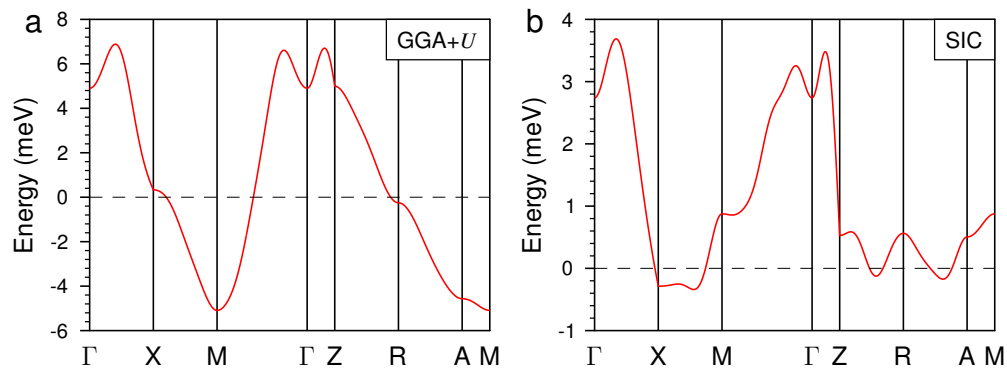


FIG. 8.  $J(\vec{Q})$  calculated along the high symmetry directions of the BZ of the tetragonal cell. The global maximum of  $J(\vec{Q})$  corresponds to the total energy minimum. Results are presented for a GGA+ $U$  (a) and self-interaction correction (SIC) (b) DFT functionals.

- GdRu<sub>2</sub>Si<sub>2</sub>, *Physica B: Condensed Matter* **222**, 80 (1996).
- [9] J. Prokleška, J. Vejpravová, and V. Sechovský, Magnetostriction measurement of GdRu<sub>2</sub>Si<sub>2</sub> single crystal, *Journal of Physics: Conference Series* **51**, 127 (2006).
- [10] J. Bouaziz, E. Mendive-Tapia, S. Blügel, and J. B. Staunton, Fermi-surface origin of skyrmion lattices in centrosymmetric rare-earth intermetallics, *Phys. Rev. Lett.* **128**, 157206 (2022).
- [11] Y. Yasui, C. J. Butler, N. D. Khanh, S. Hayami, T. Nomoto, T. Hanaguri, Y. Motome, R. Arita, T. Arima, Y. Tokura, and S. Seki, Imaging the coupling between itinerant electrons and localised moments in the centrosymmetric skyrmion magnet GdRu<sub>2</sub>Si<sub>2</sub>, *Nature Communications* **11**, 5925 (2020).
- [12] T. Nomoto, T. Koretsune, and R. Arita, Formation mechanism of the helical  $q$  structure in Gd-based skyrmion materials, *Phys. Rev. Lett.* **125**, 117204 (2020).
- [13] S. Hayami and Y. Motome, Square skyrmion crystal in centrosymmetric itinerant magnets, *Phys. Rev. B* **103**, 024439 (2021).
- [14] N. Matsuyama, T. Nomura, S. Imajo, T. Nomoto, R. Arita, K. Sudo, M. Kimata, N. D. Khanh, R. Takagi, Y. Tokura, S. Seki, K. Kindo, and Y. Kohama, Quantum oscillations in the centrosymmetric skyrmion-hosting magnet GdRu<sub>2</sub>Si<sub>2</sub>, *Phys. Rev. B* **107**, 104421 (2023).
- [15] G. Bihlmayer, P. Noel, D. V. Vyalikh, E. V. Chulkov, and A. Manchon, Rashba-like physics in condensed matter, *Nature Reviews Physics* **4**, 642 (2022).
- [16] A. I. Liechtenstein, M. I. Katsnelson, V. P. Antropov, and V. A. Gubanov, Local spin density functional approach to the theory of exchange interactions in ferromagnetic metals and alloys, *Journal of Magnetism and Magnetic Materials* **67**, 65 (1987).
- [17] M. Hoffmann, A. Ernst, W. Hergert, V. N. Antonov, W. A. Adeagbo, R. M. Geilhufe, and H. Ben Hamed, Magnetic and electronic properties of complex oxides from first-principles, *Physica Status Solidi (b)* **257**, 1900671 (2020).
- [18] M. Güttler, A. Generalov, M. M. Otrokov, K. Kummer, K. Kliemt, A. Fedorov, A. Chikina, S. Danzenbächer, S. Schulz, E. V. Chulkov, Y. M. Koroteev, N. Carocanales, M. Shi, M. Radovic, C. Geibel, C. Laubschat, P. Dudin, T. K. Kim, M. Hoesch, C. Krellner, and D. V. Vyalikh, Robust and tunable itinerant ferromagnetism at the silicon surface of the antiferromagnet GdRh<sub>2</sub>Si<sub>2</sub>, *Scientific Reports* **6**, 24254 (2016).
- [19] K. Kliemt, M. Peters, F. Feldmann, A. Kraiker, D.-M. Tran, S. Rongstock, J. Hellwig, S. Witt, M. Bolte, and C. Krellner, Crystal growth of materials with the ThCr<sub>2</sub>Si<sub>2</sub> structure type, *Cryst. Res. Technol.* **55**, 1900116 (2020).
- [20] P. E. Blöchl, Projector augmented-wave method, *Phys. Rev. B* **50**, 17953 (1994).
- [21] P. E. Blöchl, Projector augmented-wave method, *Phys. Rev. B* **50**, 17953 (1994).
- [22] G. Kresse and D. Joubert, From ultrasoft pseudopotentials to the projector augmented-wave method, *Phys. Rev. B* **59**, 1758 (1999).
- [23] G. Kresse and J. Furthmüller, Efficient iterative schemes for ab initio total-energy calculations using a plane-wave basis set, *Phys. Rev. B* **54**, 11169 (1996).
- [24] G. Kresse and D. Joubert, From ultrasoft pseudopotentials to the projector augmented-wave method, *Phys. Rev. B* **59**, 1758 (1999).
- [25] J. P. Perdew, K. Burke, and M. Ernzerhof, Generalized gradient approximation made simple, *Phys. Rev. Lett.* **77**, 3865 (1996).
- [26] A. V. Krukau, O. A. Vydrov, A. F. Izmaylov, and G. E. Scuseria, Influence of the exchange screening parameter on the performance of screened hybrid functionals, *The Journal of Chemical Physics* **125**, 224106 (2006).
- [27] V. I. Anisimov, J. Zaanen, and O. K. Andersen, Band theory and mott insulators: Hubbard  $U$  instead of Stoner  $I$ , *Phys. Rev. B* **44**, 943 (1991).
- [28] L. G. Ferreira, M. Marques, and L. K. Teles, Approximation to density functional theory for the calculation of band gaps of semiconductors, *Phys. Rev. B* **78**, 125116 (2008).
- [29] L. G. Ferreira, M. Marques, and L. K. Teles, Slater half-occupation technique revisited: the LDA-1/2 and GGA-1/2 approaches for atomic ionization energies and band gaps in semiconductors, *AIP Advances* **1**, 032119 (2011).
- [30] L. M. Sandratskii, Noncollinear magnetism in itinerant-electron systems: Theory and applications, *Advances in Physics* **47**, 91 (1998).
- [31] P. V. C. Medeiros, S. Stafström, and J. Björk, Effects of extrinsic and intrinsic perturbations on the electronic

- structure of graphene: Retaining an effective primitive cell band structure by band unfolding, *Phys. Rev. B* **89**, 041407 (2014).
- [32] P. V. C. Medeiros, S. S. Tsirkin, S. Stafström, and J. Björk, Unfolding spinor wave functions and expectation values of general operators: Introducing the unfolding-density operator, *Phys. Rev. B* **91**, 041116 (2015).
- [33] K. Koepnik and H. Eschrig, Full-Potential Nonorthogonal Local-Orbital Minimum-Basis Band-Structure Scheme, *Phys. Rev. B* **59**, 1743 (1999).
- [34] K. Momma and F. Izumi, *VESTA 3* for three-dimensional visualization of crystal, volumetric and morphology data, *Journal of Applied Crystallography* **44**, 1272 (2011).
- [35] M. Kawamura, Fermisurfer: Fermi-surface viewer providing multiple representation schemes, *Computer Physics Communications* **239**, 197 (2019).
- [36] S. L. Dudarev, G. A. Botton, S. Y. Savrasov, C. J. Humphreys, and A. P. Sutton, Electron-energy-loss spectra and the structural stability of nickel oxide: An LSDA+*U* study, *Phys. Rev. B* **57**, 1505 (1998).
- [37] J. P. Perdew and A. Zunger, Self-interaction correction to density-functional approximations for many-electron systems, *Phys. Rev. B* **23**, 5048 (1981).
- [38] M. Lüders, A. Ernst, M. Däne, Z. Szotek, A. Svane, D. Ködderitzsch, W. Hergert, B. L. Györfy, and W. M. Temmerman, Self-interaction correction in multiple scattering theory, *Phys. Rev. B* **71**, 205109 (2005).